Resistively shunted $YBa_2Cu_3O_7$ grain boundary junctions and low-noise SQUIDs patterned by a focused ion beam down to 80 nm linewidth



2011 Supercond. Sci. Technol. 24 015015

(http://iopscience.iop.org/0953-2048/24/1/015015)

Supercond. Sci. Technol. **24** (2011) 015015 (8pp) doi:10.1088/0953-2048/24/1/015015

# Resistively shunted $YBa_2Cu_3O_7$ grain boundary junctions and low-noise SQUIDs patterned by a focused ion beam down to 80 nm linewidth

**J Nagel[1], K B Konovalenko[1], M Kemmler[1], M Turad[1], R Werner[1], E Kleisz[2], S Menzel[2], R Klingeler[2], B Büchner[2], R Kleiner[1] and D Koelle[1]**

[1] Physikalisches Institut—Experimentalphysik II and Center for Collective Quantum Phenomena, Universität Tübingen, Auf der Morgenstelle 14, D-72076 Tübingen, Germany
[2] Leibniz-Institut für Festkörper- und Werkstoffforschung (IFW) Dresden, D-01171 Dresden, Germany

E-mail: koelle@uni-tuebingen.de

Received 20 September 2010, in final form 29 October 2010
Published 15 December 2010
Online at stacks.iop.org/SUST/24/015015

**Abstract**

$YBa_2Cu_3O_7$ 24° (30°) bicrystal grain boundary junctions (GBJs), shunted with 60 nm (20 nm) thick Au, were fabricated by focused ion beam milling with widths 80 nm $\leqslant w \leqslant$ 7.8 $\mu$m. At 4.2 K we find critical current densities $j_c$ in the $10^5$ A cm$^{-2}$ range (without a clear dependence on $w$) and an increase in resistance times junction area $\rho_n$ with an approximate scaling $\rho_n \propto w^{1/2}$. For the narrowest GBJs $j_c\rho_n = I_cR_n \approx 100\ \mu$V (with critical current $I_c$ and junction resistance $R_n$), which is promising for the realization of sensitive nanoSQUIDs for the detection of small spin systems. We demonstrate that our fabrication process allows the realization of sensitive nanoscale dc SQUIDs; for a SQUID with $w \approx 100$ nm wide GBJs we find an rms magnetic flux noise spectral density of $S_\Phi^{1/2} \approx 4\ \mu\Phi_0$ Hz$^{-1/2}$ in the white noise limit. We also derive an expression for the spin sensitivity $S_\mu^{1/2}$, which depends on $S_\Phi^{1/2}$, on the location and orientation of the magnetic moment of a magnetic particle to be detected by the SQUID, and on the SQUID geometry. For the unoptimized SQUIDs presented here, we estimate $S_\mu^{1/2} = 390\,\mu_B$ Hz$^{-1/2}$, which could be further improved by at least an order of magnitude.

(Some figures in this article are in colour only in the electronic version)

## 1. Introduction

There is a growing interest in developing sensitive miniaturized superconducting quantum interference devices (SQUIDs) for the investigation of small spin systems and scanning SQUID microscopy with sub-$\mu$m spatial resolution [1–3]. A main motivation is measurements on single nanomagnetic particles, and the ultimate goal is the direct detection of switching of a single electronic spin with various potential applications in spintronics, quantum computing and on biomolecules. Although sensitive spectroscopic techniques for single spin detection, such as magnetic resonance force microscopy, have been developed [4, 5], sensors for the direct detection of the switching of magnetization of small spin systems still have to be improved significantly. Using SQUIDs for this application requires the realization of sub-$\mu$m Josephson junctions and SQUID loops, both for optimum inductive coupling to nanosized objects and for improving the SQUID sensitivity for operation at switching fields of the magnetic particles up to the Tesla range at temperatures of $T \approx 4$ K and well below (see the pioneering work by Voss *et al* [6] and more recent work, e.g. [2, 7–12] and references therein). Here, we note that one of the main motivations in the field of direct detection of magnetization reversal of small spin systems is

 

the investigation of tunneling of magnetization, which however typically can be only observed at temperatures well below 4 K. This means that in this case the envisaged operation temperature for miniaturized SQUIDs is at several 100 mK or even further below [12].

Most frequently used techniques for creating superconducting sub-$\mu$m thin film structures are based on electron beam lithography, or on focused ion beam (FIB) patterning. While patterning of sub-$\mu$m SQUID loops poses no particular problems, the properties of sub-$\mu$m Josephson junctions embedded in the SQUID loop have to be carefully optimized in order to realize low-noise SQUIDs. Here, an important figure of merit is the rms spectral density of flux noise $S_\Phi^{1/2}$, which for optimized SQUIDs based on the standard Nb/$AlO_x$/Nb technology for $\mu$m-sized junctions is in the range of $\mu\Phi_0$ $Hz^{-1/2}$ ($\Phi_0$ is the magnetic flux quantum). However, critical current densities $j_c > 1$ kA $cm^{-2}$ are hard to achieve reliably with this technology, yielding too small critical currents $I_c = j_c A_J$ for junction areas $A_J$ in the $(100\ nm)^2$ range. Therefore, research focused on Nb or Al thin film constriction type junctions (with widths $w \gtrsim 50$ nm), sometimes shunted with a thin film normal metal layer (e. g. Au, or W) to ensure non-hysteretic current–voltage-characteristics ($IV$Cs) [3, 6]. This approach often produced SQUIDs with $S_\Phi^{1/2} \gtrsim 1$ m$\Phi_0$ $Hz^{-1/2}$, with a few exceptions like the early results by Voss *et al* [6], or the recent work by Hao *et al* [13] who reported on highly sensitive Nb SQUIDs with $S_\Phi^{1/2} \approx 0.2\ \mu\Phi_0\ Hz^{-1/2}$. These encouraging results have been obtained with FIB patterned constriction junctions at $T = 6.8$ K.

For operation in high magnetic fields $B$ a small junction size ($\perp \vec{B}$) is required due to the suppression of $I_c$ with increasing magnetic flux in the junction above several $\Phi_0$, which demands a particularly large $j_c$. Furthermore, the maximum field of operation is limited by the upper critical field $B_{c2}$, e.g. to $\lesssim$1 T for typical Nb thin film based SQUIDs. Here, high-transition-temperature (high-$T_c$) SQUIDs offer three advantages: (i) very high $B_{c2}$ in the tens of Tesla regime or even more, (ii) high $j_c > 10^5$ A $cm^{-2}$ for grain boundary junctions (GBJs) operating at $T = 4.2$ K and well below and (iii) a GBJ geometry with the junction barrier perpendicular to the thin film SQUID loop; this allows the application of very large in-plane fields (for switching the magnetization of nanoparticles) which do not couple to the SQUID and which do not reduce $I_c$. Here, the challenge is to produce sub-$\mu$m GBJs with high quality, in particular with high $j_c$ and $\rho_n = R_n A_J$, where $R_n$ is the junction resistance, i.e. with high $j_c \rho_n = I_c R_n$.

At this point, we should mention that, in principle, also constriction type junctions based on HTS, or $MgB_2$ thin films may fulfill the above mentioned requirements, and in fact such junctions and SQUIDs based on them have been patterned by FIB [14–18]. However, these junctions typically show flux-flow type or hysteretic $IV$Cs at low $T$, such that their operation temperature is often limited to a narrow $T$ range well above 4 K, and their performance with respect to flux noise so far has never reached the performance of high-$T_c$ low-noise GBJ SQUIDs [19]. Furthermore, we note that due to the small lower critical fields $B_{c1}$, HTS thin film SQUIDs will be in the mixed state, and strong pinning of vortices will be important, in order to keep low-frequency noise due to vortex motion as small as possible. However, the same applies to, e.g., Nb SQUIDs if they are operated above $B_{c1}$; this issue has not been studied so far, since SQUIDs usually are operated at the magnetic field of the earth or well below.

Already in the 1990s thin film high-$T_c$ $YBa_2Cu_3O_7$ (YBCO) sub-$\mu$m GBJs and SQUIDs have been fabricated using e-beam lithography [20, 21]. However, oxygen loss during processing, in particular for very thin films, may require post-deposition annealing to improve junction characteristics [22]. More recently, sub-$\mu$m YBCO GBJs have also been fabricated by FIB [23], and both technologies enabled fundamental studies on transport and noise in high-$T_c$ sub-$\mu$m GBJs [22, 24–26]. Still, a significant degradation of $j_c$ for $w \lesssim 500$ nm was found [20, 21, 23], and the use of deep sub-$\mu$m GBJs for the realization of nanoSQUIDs has not been explored yet. The motivation for the realization of sub-$\mu$m GBJs with widths well below 500 nm is based on the following considerations: first of all, operation in high magnetic fields in the Tesla range, as mentioned above, requires very accurate alignment of the applied magnetic field in the thin film plane in order to reduce coupling of the applied out-of-field component to the GBJ. This requires as small as possible GBJ widths. Furthermore, as will be shown below, the spin sensitivity scales linearly with the rms flux noise $S_\Phi^{1/2}$ of the SQUID. Optimization of $S_\Phi^{1/2}$ requires an as small as possible SQUID loop inductance $L$ [27], i.e. minimization of the dimensions of the SQUID loop, which for topological reasons has to be intersected by the grain boundary. Here, SQUID loop sizes of the order of 100 nm seem to be feasible, according to our experience on FIB patterning of our devices as described below. In order to ensure optimum SQUID performance, one should achieve at least a few SQUID modulations within the Fraunhofer-like $I_c(B)$ modulation of the single GBJs. This in turn requires also shrinking the GBJ widths down to the size of the SQUID loop. Hence, our goal is to demonstrate the feasibility of FIB patterning YBCO GBJs down to junction widths of the order of 100 nm. In order to accomplish this, we investigated the scaling behavior of YBCO GBJ properties with linewidths ranging over two orders of magnitude, from $\sim$8 $\mu$m down to 80 nm, and we investigated the electric transport and noise properties of YBCO GBJ dc SQUIDs with the smallest linewidths achieved within this study. We note that we performed so far only investigations on low-field properties of the fabricated GBJs and SQUIDs, as we are at this stage interested in clarifying the intrinsic scaling properties of our devices with GBJ width, although the ultimate goal of this work is to operate such SQUIDs in high magnetic fields in the Tesla range at $T = 4.2$ K and well below.

The remainder of this paper is organized as follows. Section 2 very briefly addresses sample fabrication and layout, including some information on the quality of our YBCO thin films. In section 3 we first describe and discuss the results of electric transport properties of our shunted GBJs, with focus on their dependence on junction width, which was varied over two orders of magnitude (3.1). The second part

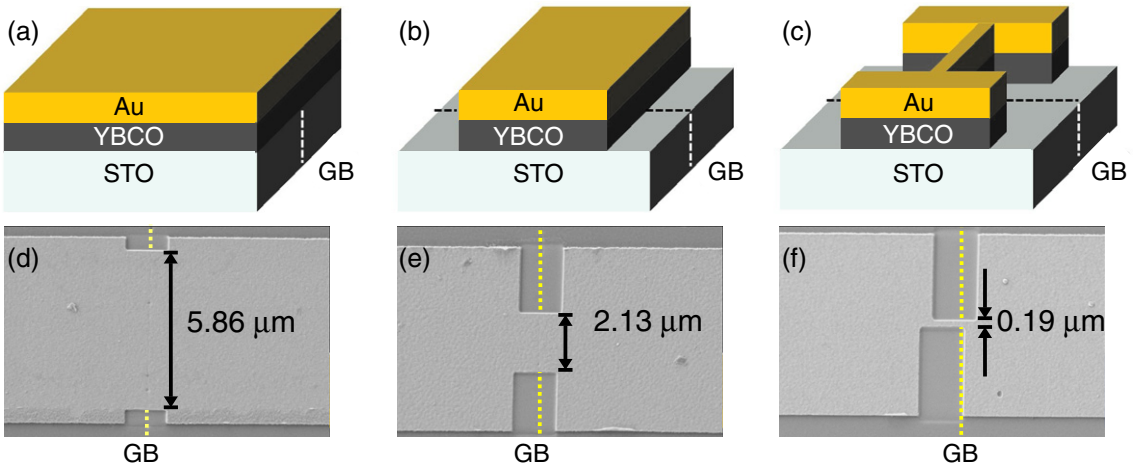


**Figure 1.** Upper row: schematic illustration of the steps used for fabricating YBCO grain boundary junctions (GBJs). (a) *In situ* deposition of a YBCO/Au bilayer on a bicrystal STO substrate; (b) patterning of 8 $\mu$m wide bridges straddling the grain boundary (GB) (by photolithography and Ar ion milling); (c) patterning of a narrow GBJ by FIB. The location of the GB is indicated by dashed lines. The bottom row (d)–(f) shows scanning electron microscopy images of three single junction devices (from *chip-1*) with different widths (indicated on the graphs).

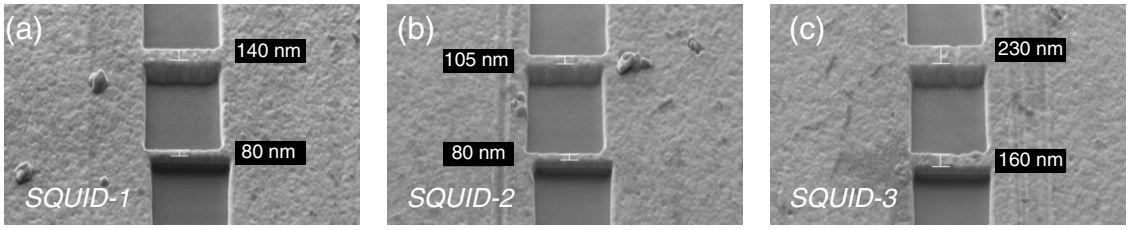


**Figure 2.** SEM images of the three SQUIDs (loop size 1.0 × 1.2 $\mu$m$^2$) fabricated on *chip-2*. Labels in black boxes give junction widths.

(3.2) of this section describes the results obtained for our SQUIDs, with focus on electric transport and noise properties of the SQUID with the smallest GBJ width used in this study (*SQUID-2*). Having characterized our SQUIDs, we discuss in section 4 the important relation between the flux noise $S_\Phi^{1/2}$ of the SQUIDs and the spin sensitivity $S_\mu^{1/2}$, which is the important figure of merit for detection of small spin particles. Here, we provide a solution for calculating the spin sensitivity for any arbitrary geometry of the SQUID loop as a function of position and orientation of the magnetic moment of a small particle to be detected. We then apply this solution to the particular geometry of *SQUID-2* and finally discuss perspectives for further optimization of $S_\mu^{1/2}$. Section 5 contains our conclusions.

## 2. Sample fabrication

We fabricated devices on $SrTiO_3$ (STO) symmetric [001] tilt bicrystal substrates with misorientation angle $\theta = 30°$ (*chip-1*) and 24° (*chip-2*). Figures 1(a)–(c) illustrate the fabrication steps. We deposited $d_Y = 50$ nm thick *c*-axis oriented epitaxially grown YBCO by pulsed laser deposition (PLD), followed by *in situ* evaporation of Au (at room temperature) with thickness $d_{Au} = 20$ nm (*chip-1*) and 60 nm (*chip-2*), serving as a resistive shunt and protection layer during FIB milling. For details on PLD growth of our YBCO films on STO substrates, and their structural and electric transport properties, see [28]. In brief, our 50 nm thick YBCO films typically yield 0.1° full width half maximum of the rocking curve at the (005) x-ray diffraction peak, have $T_c = 91$ K with a transition width ∼0.5 K and normal state resistivity $\rho \approx 50$ $\mu\Omega$ cm at $T = 100$ K. On both chips, 8 $\mu$m wide bridges straddling the grain boundary were fabricated by photolithography and Ar ion milling and then patterned by FIB with Ga ions (50 pA, 30 kV) to make junctions and dc SQUIDs with junction widths 80 nm $\leqslant w \leqslant$ 7.8 $\mu$m. FIB patterning was performed with a dual beam 1540 XB cross beam (Zeiss). This allowed us to apply an optimized FIB cut procedure (soft FIB procedure), with small ion current density and minimum ion exposure time of non-milled areas, i.e. only very brief snapshot imaging prior to milling. Even for imaging by the electron beam, we minimized the exposure time in order to avoid damage of our FIB cut bridges. Figures 1(d)–(f) show scanning electron microscopy (SEM) images of three GBJs fabricated on *chip-1*. In total, we investigated 22 single GBJs and three dc SQUIDs (on *chip-2*; hole size 1.0 × 1.2 $\mu$m$^2$). SEM images of the three SQUIDs are shown in figure 2.

## 3. Experiments

We characterized our devices at $T = 4.2$ K in a magnetically shielded environment. All results shown below have been

obtained under these conditions. For measurements of $IV$Cs, $I_c(B)$ and $V(B)$ we used a four-point arrangement with a room temperature voltage amplifier. For SQUID noise measurements we preamplified the output signal with a Nb dc SQUID amplifier with 0.1 nV Hz$^{-1/2}$ resolution. For noise measurements, the YBCO SQUID was operated open-loop, i.e. we applied a constant bias current and constant flux bias, and we detected the voltage across the SQUID by connecting voltage leads to the input coil which was inductively coupled to a Nb dc SQUID; a 10 Ω resistor (also at 4.2 K) was in series with the input coil. The Nb SQUID was read out in a flux-locked loop with ac flux bias at modulation frequency $f_{\rm mod} = 256$ kHz (PC-1000 Multi-Channel dc SQUID Electronics System with SQ100 SQUID-Sensor from STAR Cryoelectronics).

### *3.1. Transport properties versus junction width*

All devices showed resistively-and-capacitively-shunted-junction (RCSJ)-type $IV$Cs, which for some of the sub-$\mu$m junctions on *chip-1* (thinner Au shunt) had a small hysteresis. Therefore, for *chip-2*, we increased $d_{\rm Au}$ by a factor of three, yielding non-hysteretic $IV$Cs, except for the 530 nm wide junction, which has an exceptionally high $j_c\rho_n$. From the $IV$Cs we determined $I_c$, and $R_n$, and calculated $j_c$ and $\rho_n$, using $d_Y = 50$ nm and $w$ as obtained from SEM images. The results of these measurements are summarized in figure 3, plotted versus $w$ which spans two orders of magnitude. The full symbols in figure 3 show data obtained after FIB patterning; the open symbols show data (for *chip-2*) from the 8 $\mu$m wide bridges prior to FIB patterning.

Figure 3(a) shows $j_c(w)$, which is well above $10^5$ A cm$^{-2}$ over the entire range of $w$. The $j_c$ values shown are typical for $\theta = 24°$ and 30° YBCO GBJs at 4.2 K and $w \gtrsim 2$ $\mu$m [19]; however, such high $j_c$ values have not been previously observed for widths down to 80 nm. We do find a significant scattering of $j_c(w)$, however without a clear width dependence. The average $j_c$ for *chip-2* is 1.5 times the one for *chip-1*, as expected from the scaling $j_c(\theta)$ of GBJs [29]. The comparison of $j_c$ of the same bridges before and after FIB patterning shows that for most devices $j_c$ even slightly increased after FIB patterning. The positions of the devices on *chip-2* (along the GB of the substrate) are ordered according to their device number (1–15) (cf top axis of figure 3(a)) from the left to the right edge of the substrate. There is a clear trend of increasing $j_c$ by about a factor of two (for the 8 $\mu$m wide bridges) along the entire substrate. The origin of this gradient in $j_c$ has not been clarified; however we can rule out a corresponding variation in the YBCO film thickness across the substrate. A possible explanation for the observed gradient in $j_c$ of the 8 $\mu$m wide GBJs along *chip-2* could be a gradient in the quality of the GB in the bicrystal substrate, which in turn can cause a gradient in the barrier thickness of the GBJs along the chip.

Figure 3(b) shows an approximate scaling $\rho_n \propto \sqrt{w}$ of unclear origin. We note that the lines shown in figures 3(b) and (c) are not fits to our data. These lines are just drawn to illustrate the trend of decreasing resistivity $\rho_n$ with decreasing

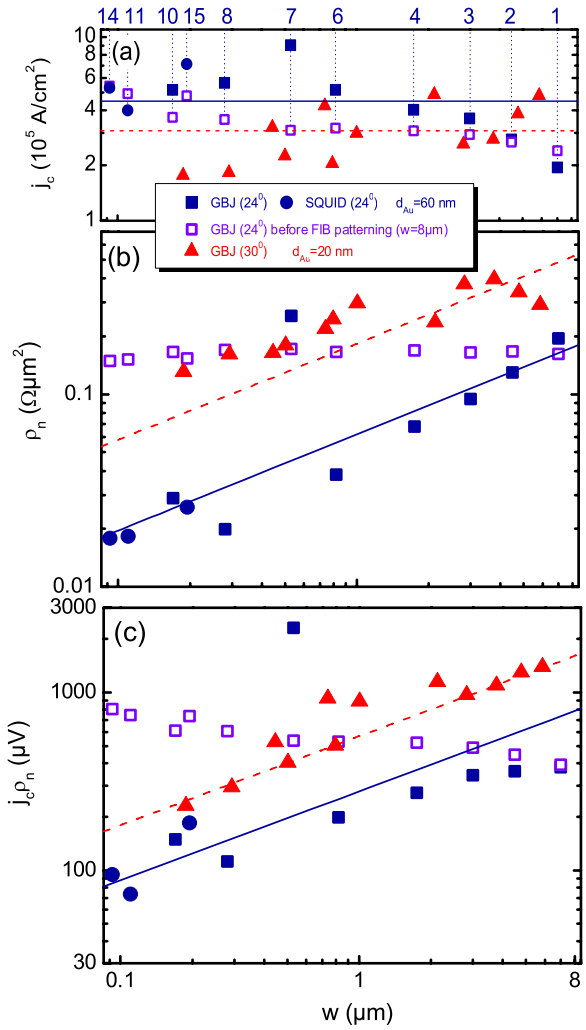


**Figure 3.** Transport data of YBCO GBJs and SQUIDs versus junction width $w$ (solid symbols): (a) critical current density $j_c(w)$; (b) junction resistance times area $\rho_n(w)$; (c) $j_c\rho_n(w)$. Dashed (solid) lines indicate average $j_c$ values (in (a)) and approximate scaling of $\rho_n(w)$ (in (b)) and $j_c\rho_n(w)$ (in (c)) for *chip-1* (*chip-2*). Open squares are data for the same GBJs on *chip-2*, measured prior to FIB patterning (i.e. $w = 8$ $\mu$m). The numbers on the top axis in (a) label the device numbers on *chip-2*.

junction width $w$. Before FIB patterning, the 8 $\mu$m wide GBJs on *chip-2* all had $\rho_n \approx 0.17\,\Omega\ \mu$m$^2$, which falls onto the observed $\rho_n(w)$ dependence, indicating that this scaling is not specific to FIB patterned GBJs. Furthermore, $\rho_n \approx 0.17\,\Omega\ \mu$m$^2$ is an order of magnitude below typical values for unshunted GBJs [29], which we attribute to the Au shunt, and which is also consistent with the larger $\rho_n$ of GBJs on *chip-1* with thinner Au. For *chip-1*, $d_{\rm Au} = 20$ nm is close to the 15 nm implantation depth of 30 keV Ga ions in Au [30]. Hence one might expect that FIB induces an increase in the Au resistivity via Ga implantation. This effect should be suppressed for *chip-2* with three times thicker Au. In any case, it is hard to explain why Ga implantation should increase $\rho_n$ for wider junctions. Certainly, Ga implantation is not the only detrimental effect of FIB patterning. In particular, the Ga beam might destroy the crystalline order close to the patterned edges. However, our

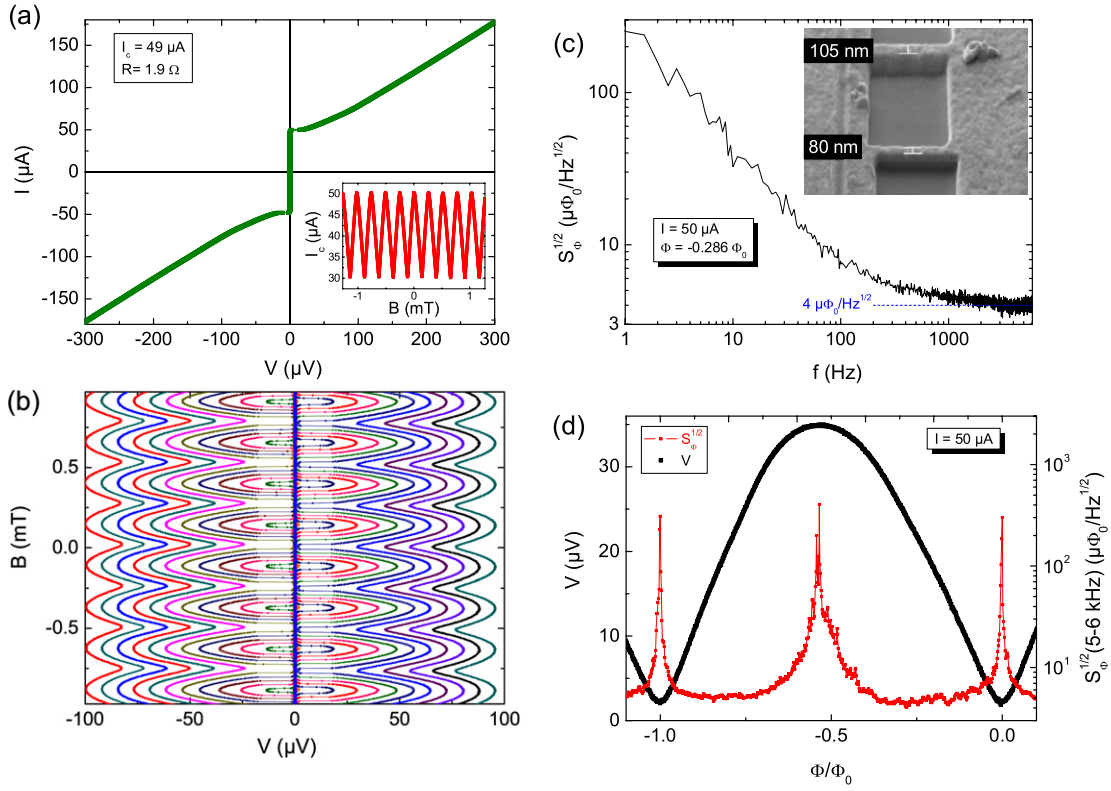


**Figure 4.** Transport and noise characteristics of *SQUID-2*. (a) $IVC$ at $B = 0$; the inset shows $I_c(B)$. (b) $V(B)$ for $I = -70.8$ to $-12.3$ and 10.0–68.5 $\mu$A (in 3.9 $\mu$A steps). (c) Spectral density of rms flux noise $S_\Phi^{1/2}(f)$; inset: SEM image of the SQUID. (d) $V(\Phi)$ and $S_\Phi^{1/2}(\Phi)$ (averaged from $f = 5$ to 6 kHz).

experimental observation of almost constant $j_c$ for GBJ widths down to 80 nm rules out severe edge damage effects on a length scale of several tens of nm. This observation also rules out such effects as a possible explanation for the observed scaling behavior of $\rho_n(w)$. Certainly, the optimization of the transport properties of our shunted YBCO GBJs needs further detailed analysis, such as, e.g., shown in [31].

Figure 3(c) shows $j_c\rho_n(w) \approx 0.1$–1 mV, i.e. at least one order of magnitude below the values for unshunted YBCO GBJs of comparable $j_c$. This is certainly due to the suppression of $j_c\rho_n$ by the Au shunt required to ensure non-hysteretic $IVC$s at 4.2 K. The decrease of $j_c\rho_n$ with decreasing $w$ is due to the scaling of $\rho_n(w)$ mentioned above. Still, even for the 80 nm wide GBJs we find reasonable values of $j_c\rho_n$ around 100 $\mu$V, which are certainly quite suitable for the realization of sensitive SQUIDs.

### *3.2. SQUID parameters, transport characteristics and noise performance*

The results of transport measurements on all three SQUIDs (on *chip-2*) are summarized in table 1. The SQUID inductance $L$ was calculated with the numerical simulation software 3D-MLSI [32], which is based on a finite element method to solve the London equations for a given film thickness and London penetration depth ($d_Y = 50$ nm and $\lambda_L = 140$ nm, respectively, in our case). As $d_Y \ll \lambda_L$, the kinetic inductance contributes significantly to $L$. For *SQUID-1* and *SQUID-2*, the

**Table 1.** Parameters of YBCO GBJ dc SQUIDs.

| # | $w_1$ (nm) | $w_2$ (nm) | $I_c$ ($\mu$A) | $R_n$ ($\Omega$) | $I_cR_n$ ($\mu$V) | $L$ (pH) | $\beta_L$ | $V_\Phi$ (mV/$\Phi_0$) |
|---|---|---|---|---|---|---|---|---|
| 1 | 80 | 140 | 44 | 1.7 | 73 | 15 | 0.31 | 0.08 |
| 2 | 80 | 105 | 49 | 1.9 | 94 | 16 | 0.38 | 0.11 |
| 3 | 160 | 230 | 139 | 1.3 | 185 | 10 | 0.66 | 0.13 |

GBJ widths $w_i$ ($i = 1, 2$) are below $\lambda_L$, which increases $L$ over that of *SQUID-3* with wider junctions. From the calculated $L$ and measured $I_c$ we obtain $\beta_L \equiv LI_c/\Phi_0 \approx 0.3$–0.7, i.e. not far from the optimum value $\beta_L \approx 1$ [33]. The transfer function $V_\Phi$, i.e. the slope of the $V(\Phi)$ curves at optimum bias current and applied flux $\Phi = \pm\frac{1}{4}\Phi_0$, is around 0.1 mV/$\Phi_0$, and the effective area $A_{\rm eff} = \Phi/B \approx 8\ \mu{\rm m}^2$ for all three SQUIDs.

Figure 4 shows electric transport and noise data obtained for *SQUID-2* (the device with smallest $w$; see inset in (c)). Figure 4(a) shows an $IVC$ for an applied field $B = 0$ corresponding to a maximum in $I_c$. The small jump at $I_c$ to $V \neq 0$ indicates that the junctions are at the transition to the underdamped regime. The inset in figure 4(a) shows $I_c(B)$ with 40% modulation. Figure 4(b) shows $V(B)$ for various bias currents $I$. The small shift in the minima of $V(B)$ upon reversing $I$ is in accordance with the $I_c$ asymmetry of the two GBJs due to their different widths.

Finally, graphs (c) and (d) in figure 4 show the results of noise measurements on *SQUID-2*. Figure 4(c) shows the rms spectral density of flux noise $S_\Phi^{1/2}(f) \propto f^{-x}$ for optimum

flux bias $\Phi = -0.286\Phi_0$ with $x \approx 0.8$ for frequencies $f \lesssim 100$ Hz. The relatively small width (8 $\mu$m) of the structures adjacent to the SQUID (cooled and operated in magnetically shielded environment) makes it quite unlikely that Abrikosov vortices are trapped there and cause excess low-frequency noise due to vortex hopping. Instead, it is much more likely that the excess low-frequency noise is due to $I_c$ fluctuations in the GBJs [19]. For larger $f$ we find a white flux noise level $S_{\Phi,w}^{1/2} \approx 4\ \mu\Phi_0\ \mathrm{Hz}^{-1/2}$, which to our knowledge is the lowest value of $S_\Phi^{1/2}$ obtained for a YBCO dc SQUID with sub-$\mu$m GBJs so far. Figure 4(d) shows the rms flux noise $S_\Phi^{1/2}$ (averaged from $f = 5$ to 6 kHz) and the SQUID voltage $V$ versus applied flux $\Phi$. We find a rather shallow minimum in $S_\Phi^{1/2}(\Phi)$ for an applied flux where the slope of the $V(\Phi)$ curve (also shown in graph (d)) is close to its maximum. We note that the need to resistively shunt the junctions for low-$T$ operation leads to a reduction in $I_c R_n$, which in turn reduces the transfer function $V_\Phi \propto R_n$ and also increases the flux noise $S_\Phi \propto 1/R$ of the SQUIDs. On the other hand, operation at lower $T$ will reduce the Nyquist noise from the shunt resistors and hence improve $S_\Phi$ [34]. Certainly, the optimization of the flux noise of the SQUIDs will require further analysis, e.g. by comparing experimental results with numerical simulations based on the RCSJ model [19, 34].

## 4. Spin sensitivity

Coming back to the main motivation of this work, i.e. the development of nanoSQUIDs for the detection of small spin systems, we derive an expression for the spin sensitivity $S_\mu^{1/2}$, which we then use to calculate $S_\mu^{1/2}$ for the particular geometry and flux noise of *SQUID-2* as a function of the position of a magnetic particle for a given orientation of its magnetic moment. $S_\mu$ is the spectral density of spin noise, which depends on the spectral density of flux noise $S_\Phi$ of the SQUID and on the coupling between a magnetic particle with magnetic moment $\vec{\mu} = \mu \cdot \hat{e}_\mu$ and the SQUID via the relation $S_\mu = S_\Phi/\phi_\mu^2$. Here, $\phi_\mu(\hat{e}_\mu, \vec{r}_\mu) \equiv \Phi_\mu(\vec{\mu}, \vec{r}_\mu)/\mu$ is the magnetic flux $\Phi_\mu$ per magnetic moment $\mu$ coupled into the SQUID loop by the magnetic particle, which is located at the position $\vec{r}_\mu$ and which is oriented along $\hat{e}_\mu$. This means that, in order to determine $S_\mu^{1/2}$ for a given $S_\Phi^{1/2}$, one needs to calculate the coupling function $\phi_\mu(\hat{e}_\mu, \vec{r}_\mu)$, which will also depend on the SQUID geometry.

To determine $\phi_\mu$, we assume that the magnetic moment $\vec{\mu}$ is moved from a distance far away to a position $\vec{r} = \vec{r}_\mu$ close to the SQUID loop. When the magnetic moment approaches $\vec{r}_\mu$, a circulating current $I_\mu(\vec{\mu}, \vec{r}_\mu)$ is induced in the SQUID loop, which compensates the coupled flux $\Phi_\mu$, due to the diamagnetic response of the SQUID loop. The magnetic field energy stored in the loop of inductance $L$ is $W_{\mathrm{loop}} = \frac{1}{2} L I_\mu^2$. The work required to place the particle in the magnetic field $\vec{B}_\mu(\vec{r})$ produced by the circulating current $I_\mu$ is $W_\mu = -\frac{1}{2}\vec{\mu} \cdot \vec{B}_\mu(I_\mu, \vec{r}_\mu)$. We note that $W_\mu > 0$, due to the diamagnetic response of the SQUID loop. Hence, the total work required to bring the magnetic particle to the position $\vec{r}_\mu$ is

$$W_1 = W_{\mathrm{loop}} + W_\mu = \tfrac{1}{2} L I_\mu^2 - \tfrac{1}{2}\vec{\mu} \cdot \vec{B}_\mu(I_\mu, \vec{r}_\mu). \qquad (1)$$

On the other hand, instead of the SQUID, we may consider a fixed current system producing the same field $\vec{B}_\mu(I_\mu, \vec{r}_\mu)$ as the SQUID, when the particle is in its final position $r_\mu$. In this case, the particle has a (positive) energy

$$W_2 = -\vec{\mu} \cdot \vec{B}_\mu(I_\mu, \vec{r}_\mu). \qquad (2)$$

From $W_1 = W_2$ we obtain $I_\mu^2 = -\vec{\mu} \cdot \vec{B}_\mu / L$. With $\Phi_\mu = L I_\mu$ and with $\vec{B}_\mu / I_\mu = \vec{B}/I \equiv \vec{b}$ one thus obtains

$$\frac{\Phi_\mu(\vec{\mu}, \vec{r}_\mu)}{\mu} \equiv \phi_\mu(\hat{e}_\mu, \vec{r}_\mu) = -\hat{e}_\mu \cdot \vec{b}(\vec{r}_\mu), \qquad (3)$$

where $I$ is an arbitrary current circulating in the SQUID loop, which generates the magnetic field $\vec{B}(I)$ at the position $\vec{r}_\mu$ of the magnetic particle.

Equation (3) reproduces the results of [8, 10, 35], derived for a circular filamentary SQUID loop. Moreover, equation (3) provides a solution of the problem, valid for any *arbitrary* geometry of the superconducting loop, if one can find the normalized magnetic field distribution $\vec{b}(\vec{r})$ outside the SQUID loop. For a given $\vec{b}(\vec{r})$ (determined by the SQUID geometry only) and given flux noise, one can use equation (3) to easily calculate the spin sensitivity $S_\mu^{1/2} = S_\Phi^{1/2}/\phi_\mu$ for any orientation $\hat{e}_\mu$ and location of the magnetic particle.

For the geometry of *SQUID-2*, we calculated the spatial distribution of the current density in the SQUID loop and the corresponding three-dimensional magnetic field distribution $\vec{b}(\vec{r})$ outside the SQUID loop with 3D-MLSI [32]. Figure 5 shows the resulting spin sensitivity of *SQUID-2* (with $S_\Phi^{1/2} = 4\,\mu\Phi_0\ \mathrm{Hz}^{-1/2}$) for the detection of a magnetic particle located in the $(x, z)$ plane (at $y = 0$) with its magnetic moment pointing along the $x$ direction, i.e. $\hat{e}_\mu = \hat{e}_x$. That is, the magnetic moment of the particle is aligned parallel to the thin film plane of the SQUID, and perpendicular to the current through the GBJs.

The contour plot of the spin sensitivity shows clear minima right above the superconducting bridges straddling the grain boundary. The upper graph shows a line scan $S_\mu^{1/2}(x)$ of the spin sensitivity at a height $z = d_{\mathrm{Au}} + d_{\mathrm{Y}}/2 = 85$ nm above the ring (i.e. for our SQUID the minimum vertical distance due to the Au layer on top of the YBCO film). The lowest value of the spin sensitivity along this line scan is 390 $\mu_{\mathrm{B}}\ \mathrm{Hz}^{-1/2}$, which could be further improved by reducing the thickness of the Au layer. This can be done even without affecting the GBJ properties if the Au layer is not removed right above the GBJ. Removing the gold layer (and placing the magnetic particle at $z = d_{\mathrm{Y}}/2 = 25$ nm) would improve $S_\mu^{1/2}$ by more than a factor of two down to 180 $\mu_{\mathrm{B}}\ \mathrm{Hz}^{-1/2}$, as can be seen in the right graph, which shows the vertical dependence $S_\mu^{1/2}(z)$ at $x = 0.63$ $\mu$m, i.e. right above the center of the YBCO bridge. Moreover, further improvements in $S_\mu^{1/2}$ are feasible by improving $S_\Phi^{1/2}$, which is by no means optimized for the SQUIDs presented here. For example, our FIB technology allows for a reduction in the size of the SQUID loop down to $\sim$100 nm and a concomitant reduction in SQUID inductance $L$ down to $\sim$1 pH. This, in turn, can lead to a significant improvement in $S_\Phi^{1/2}$ by at least an order of magnitude, which would bring $S_\mu^{1/2}$ down to $\approx$20 $\mu_{\mathrm{B}}\ \mathrm{Hz}^{-1/2}$.

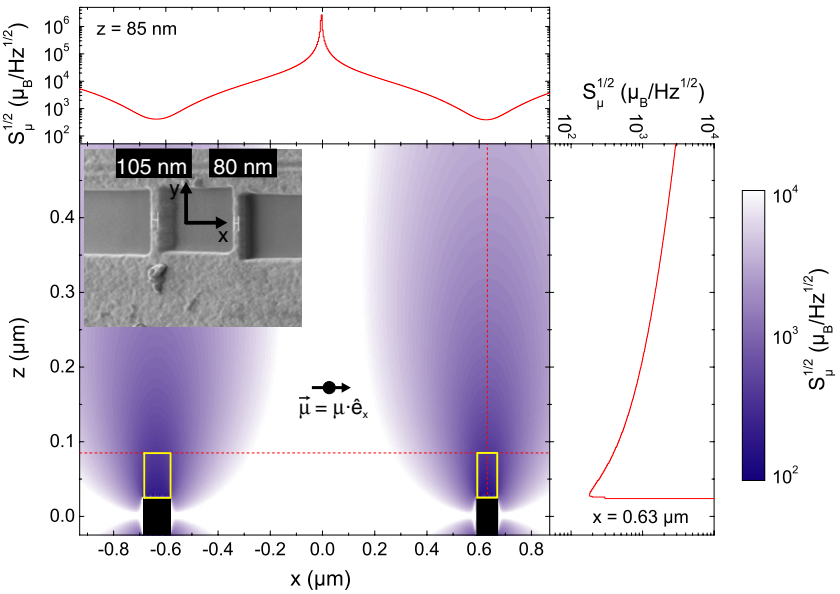


**Figure 5.** Calculated spin sensitivity $S_\mu^{1/2}$ for *SQUID-2* with $S_\Phi^{1/2} = 4\ \mu\Phi_0\ \mathrm{Hz}^{-1/2}$ for the detection of the magnetic moment of a small spin particle aligned along the $x$ axis in the $(x, y)$ plane of the SQUID loop (cf inset in main graph). The main graph shows a contour plot of $S_\mu^{1/2}$ as a function of the position of the particle in the $(x, z)$ plane at $y = 0$. The location of the YBCO bridges is indicated by the black rectangles; the rectangles (yellow lines) on top of them indicate the position of the Au layer. The line scan above the main graph shows $S_\mu^{1/2}(x)$ for $z = 85$ nm, and the line scan to the right of the main graph shows $S_\mu^{1/2}(z)$ for $x = 0.63\ \mu$m. The locations of these line scans are indicated by the dashed (red) lines in the main graph.

## 5. Conclusions

In conclusion, we have fabricated YBCO grain boundary junctions and dc SQUIDs by FIB patterning with junction widths ranging from 7.8 $\mu$m down to 80 nm. Using an Au thin film shunt on top of the junctions, we achieved non-hysteretic current–voltage-characteristics for operation of YBCO dc SQUIDs at 4.2 K and below. We demonstrated that FIB pattering enables the fabrication of deep sub-$\mu$m GBJs without degradation of critical current densities, and comparable to GBJs with widths above 1 $\mu$m. We do find a systematic dependence of the resistance times area $\rho_n$ of our GBJs, which scales approximately with the junction width $w$ as $\rho_n \propto \sqrt{w}$. The origin of this scaling could not be resolved and requires further studies. Still, we obtain values of $I_c R_n$ for our GBJs around 100 $\mu$V for junctions on the 100 nm scale, which is promising for the fabrication of sensitive nanoSQUIDs. We demonstrated low-noise performance for such devices in the $\mu\Phi_0\ \mathrm{Hz}^{-1/2}$ range, which still can be improved significantly, in particular by reducing the size of the SQUID loop and hence the SQUID inductance, and which makes them promising candidates for applications in magnetic nanoparticle detection and measurements at high magnetic fields. Certainly, the next step will be to investigate the electric transport and noise properties of optimized YBCO nanoSQUIDs in strong magnetic fields, up to above 1 T. Several issues may play an important role here, like low-frequency excess noise due to motion of Abrikosov vortices, or proper alignment of the large applied (in-plane) magnetic field, which should be perpendicular to the plane of the grain boundary in order to avoid suppression of the critical current. In the latter case, the impact of faceting of the GBJs [29] may also become important, which has to be studied in high fields. Our very preliminary studies of high-field operation of YBCO GBJ SQUIDs with 2 $\mu$m wide junctions demonstrate that such devices can operate in large in-plane fields of 1 T [36]. The presented solution for calculating the spin sensitivity for arbitrary SQUID geometries—as a function of position and orientation of the magnetization of small spin particles—provides an important tool for the systematic optimization of the spin sensitivity using nanoSQUIDs as sensitive devices for direct detection of magnetization switching of small spin particles. If the expected spin sensitivity for optimized YBCO GBJ SQUIDs can be reached at strong magnetic fields, these sensors should be clearly superior to commonly used Hall sensors [5].

## Acknowledgments

We gratefully acknowledge Thomas Dahm for helpful discussions. J Nagel and M Kemmler acknowledge support by the Carl-Zeiss Stiftung, K Konovalenko acknowledges support by the Otto Benecke Stiftung and R Werner acknowledges support by the Cusanuswerk, Bischöfliche Studienförderung. This work was funded by the Deutsche Forschungsgemeinschaft (DFG) via the SFB/TRR 21.

## References

[1] Wernsdorfer W, Mailly D and Benoit A 2000 Single nanoparticle measurement techniques *J. Appl. Phys.* **87** 5094–6

[2] Gallop J 2003 SQUIDs: some limits to measurement *Supercond. Sci. Technol.* **16** 1575–82

[3] Foley C P and Hilgenkamp H 2009 Why nanoSQUIDs are important: an introduction to the focus issue *Supercond. Sci. Technol.* **22** 064001

[4] Rugar D, Budakian R, Mamin H J and Chui B W 2004 Single spin detection by magnetic resonance force microscopy *Nature* **430** 329–32

[5] Degen C 2008 Nanoscale magnetometry: microscopy with single spins *Nat. Nanotechnol.* **3** 643–4

[6] Voss R F, Laibowitz R B and Broers A N 1980 Niobium nanobridge dc SQUID *Appl. Phys. Lett.* **37** 656–8

[7] Troeman A G P, Derking H, Borger B, Pleikies J, Veldhuis D and Hilgenkamp H 2007 NanoSQUIDs based on niobium constrictions *Nano Lett.* **7** 2152–6

[8] Granata C, Esposito E, Vettoliere A, Petti L and Russo M 2008 An integrated superconductive magnetic nanosensor for high-sensitivity nanoscale applications *Nanotechnology* **19** 275501

[9] Bouchiat V 2009 Detection of magnetic moments using a nano-squid: limits of resolution and sensitivity in near-field squid magnetometry *Supercond. Sci. Technol.* **22** 064002

[10] Tilbrook D L 2009 Nano SQUID sensitivity for isolated dipoles and small spin populations *Supercond. Sci. Technol.* **22** 064003

[11] Vohralik P F and Lam S K H 2009 NanoSQUID detection of magnetization from ferritin nanoparticles *Supercond. Sci. Technol.* **22** 064007

[12] Wernsdorfer W 2009 From micro- to nano-SQUIDs: applications to nanomagnetism *Supercond. Sci. Technol.* **22** 064013

[13] Hao L, Macfarlane J C, Gallop J C, Cox D, Beyer J, Drung D and Schurig T 2008 Measurement and noise performance of nano-superconducting-quantum-interference devices fabricated by focused ion beam *Appl. Phys. Lett.* **92** 192507

[14] Blank D H A, Booij W, Hilgenkamp H, Vulink B, Veldhuis D and Rogalla H 1995 $YBa_2Cu_3O_7$ nano-bridge junctions and dc SQUIDs made by focused ion beam milling *IEEE Trans. Appl. Supercond.* **5** 2786–9

[15] Pedyash M V, Blank D H A and Rogalla H 1996 Superconducting quantum interference devices based on YBaCuO nanobridges *Appl. Phys. Lett.* **68** 1156–8

[16] Brinkman A, Veldhuis D, Mijatovic D, Rijnders G, Blank D H A, Hilgenkamp H and Rogalla H 2001 Superconducting quantum interference device based on $MgB_2$ nanobridges *Appl. Phys. Lett.* **79** 2420

[17] Burnel G, Kang D-J, Ansell D A, Lee H-N, Moon S-H, Tarte E J and Blamire M G 2002 Directly coupled superconducting quantum interference device magnetometer fabricated in magnesium diboride by focused ion beam *Appl. Phys. Lett.* **81** 102

[18] Wu C H, Chou Y T, Kuo W C, Chen J H, Wang L M, Chen J C, Chen K L, Sou U C, Yang H C and Jeng J T 2008 Fabrication and characterization of high-$T_c$ $YBa_2Cu_3O_{7-x}$ nanoSQUIDs made by focused ion beam milling *Nanotechnology* **19** 315304

[19] Koelle D, Kleiner R, Ludwig F, Dantsker E and Clarke J 1999 High-transition-temperature superconducting quantum interference devices *Rev. Mod. Phys.* **71** 631–86

[20] Kawasaki M, Chaudari P, Newman T H and Gupta A 1991 Submicron $YBa_2Cu_3O_{7-\delta}$ grain boundary junction dc SQUIDs *Appl. Phys. Lett.* **58** 2555–7

[21] Elsner H, Ijsselsteijn R, Morgenroth W, Roth H and Meyer H G 1998 Submicrometer patterning of $YBa_2Cu_3O_{7-x}$ *Microelectron. Eng.* **41/42** 407–10

[22] Herbstritt F, Kemen T, Alff L, Marx A and Gross R 2001 Transport and noise characteristics of submicron high-temperature superconductor grain-boundary junctions *Appl. Phys. Lett.* **78** 955

[23] Testa G, Monaco A, Sarnelli E, D'Agostino A, Kang D-J, Tarte E J, Mennema S H, Bell C and Blamire M G 2004 Submicron $YBa_2Cu_3O_{7-x}$ bicrystal grain boundary junctions by focused ion beam *Supercond. Sci. Technol.* **17** 287–90

[24] Il'ichev E *et al* 2001 Degenerate ground state in a mesoscopic $YBa_2Cu_3O_{7-x}$ grain boundary Josephson junction *Phys. Rev. Lett.* **86** 5369–72

[25] Tzalenchuk A Ya, Lindström T, Charlebois S A, Stepantsov E A, Ivanov Z and Zagoskin A M 2003 Mesoscopic Josephson junctions of high-$T_c$ superconductors *Phys. Rev.* B **68** 100501(R)

[26] Testa G, Sarnelli E, Monaco A, Esposito E, Ejmaes M, Kang D-J, Mennema S H, Tarte E J and Blamire M G 2005 Evidence of midgap-state-mediated transport in 45° symmetric [001] tilt $YBa_2Cu_3O_{7-x}$ bicrystal grain-boundary junctions *Phys. Rev.* B **71** 134520

[27] Tesche C D and Clarke J 1977 DC SQUID: noise and optimization *J. Low Temp. Phys.* **29** 301–31

[28] Werner R *et al* 2010 $YBa_2Cu_3O_7/La_{0.7}Ca_{0.3}MnO_3$ bilayers: interface coupling and electric transport properties *Phys. Rev.* B **82** 224509

[29] Hilgenkamp H and Mannhart J 2002 Grain boundaries in high-$T_c$ superconductors *Rev. Mod. Phys.* **74** 485

[30] Rubanov S and Munroe P R 2003 The effect of the gold sputter-coated films in minimising damage in FIB-produced TEM specimens *Mater. Lett.* **57** 2238–41

[31] Klushin A, Golubov A, Prusseit W and Kohlstedt H 1997 Comparative study of shunted bicrystal Josephson junctions *J. Low Temp. Phys.* **106** 265–9

[32] Khapaev M, Kupriyanov M, Goldobin E and Siegel M 2003 Current distribution simulation for superconducting multi-layered structures *Supercond. Sci. Technol.* **16** 24–7

[33] Kleiner R, Koelle D, Ludwig F and Clarke J 2004 Superconducting QUantum interference devices: state-of-the-art and applications *Proc. IEEE* **92** 1534–48

[34] Chesca B, Kleiner R and Koelle D 2004 SQUID theory *The SQUD Handbook* vol 1 *Fundamentals and Technology of SQUIDs and SQUID Systems* ed J Clarke and A I Braginski (Weinheim: Wiley–VCH) chapter 2, pp 29–92

[35] Ketchen M, Awschalom D, Gallagher W, Kleinsasser A, Sandstrom R, Rozen J and Bumble B 1989 Design, fabrication, and performance of integrated miniature SQUID susceptometers *IEEE Trans. Magn.* **25** 1212–5

[36] Bushev P *et al* 2010 Trapped electron coupled to superconducting devices arXiv:1009.3425v1 [cond-mat.supr-con]